Ultrahigh-frequency surface acoustic wave transducers on ZnO/$SiO_2$/Si using nanoimprint lithography



2012 Nanotechnology 23 315303

(http://iopscience.iop.org/0957-4484/23/31/315303)

Nanotechnology **23** (2012) 315303 (10pp) doi:10.1088/0957-4484/23/31/315303

# Ultrahigh-frequency surface acoustic wave transducers on ZnO/$SiO_2$/Si using nanoimprint lithography

**S Büyükköse[1], B Vratzov[2], D Ataç[1], J van der Veen[1], P V Santos[3] and W G van der Wiel[1]**

[1] NanoElectronics Group, MESA+ Institute for Nanotechnology, University of Twente, PO Box 217, 7500 AE Enschede, The Netherlands
[2] NT&D—Nanotechnology and Devices, Wirichsbongardstraße 24, 52062 Aachen, Germany
[3] Paul-Drude-Institut für Festkörperelektronik, Hausvogteiplatz 5-7, 10117 Berlin, Germany

E-mail: s.buyukkose@utwente.nl

Received 14 May 2012, in final form 26 June 2012
Published 17 July 2012
Online at stacks.iop.org/Nano/23/315303

**Abstract**
Ultrahigh-frequency surface acoustic wave devices were fabricated on a ZnO/$SiO_2$/Si substrate using step-and-flash nanoimprint lithography combined with hydrogen silsesquioxane (HSQ) planarization. Excellent critical dimension control was demonstrated for interdigital transducers with finger electrode widths from 125 down to 65 nm. Fundamental and higher-order Rayleigh modes up to 16.1 GHz were excited and detected, which is the highest frequency for ZnO-based transducers on silicon reported so far. Surface acoustic modes were confirmed with numerical simulations. Simulation results showed good agreement with the experimental data.

(Some figures may appear in colour only in the online journal)

## 1. Introduction

Surface acoustic waves (SAWs) are widely applied in both research and industry. Their unique properties make them suitable not only for electrical signal processing, but also for other applications such as sensing [1]. Among the most exciting applications of SAWs are acousto-optical modulators as well as the control of excitons, electrons, and spins [2–5] in semiconductors. For almost all SAW applications, there is a strong demand for higher frequencies, for example to enhance processing speed or to reach the quantum regime. In the case of piezoelectric substrates, SAWs can be excited by interdigital transducers (IDTs): two interlocking comb-shaped metallic electrodes. When a radio frequency (RF) signal is applied to such an IDT, a SAW is generated when the condition $\lambda = v_{\mathrm{SAW},m}/f$ is met. Here, $\lambda$, $v_{\mathrm{SAW},m}$ and $f$ are the IDT period, the velocity of a certain SAW mode $m$, and the applied frequency, respectively.

There are two main factors determining the IDT resonant frequencies: the acoustic properties of the (piezoelectric) substrate, and the IDT period, constrained by lithography resolution. Single-crystal piezoelectric substrates such as quartz, lithium niobate ($LiNbO_3$), and lithium tantalate ($LiTaO_3$) are often used because of their high electromechanical coupling coefficients, advantageous for converting the energy of the RF excitation into mechanical energy of the SAW. However, their SAW velocities are relatively low, limiting the operating frequency [6]. Substrates with overlayers of different materials with sharply varying elastic properties offer an alternative to get higher frequencies, as they enable the excitation of higher-order SAW modes with higher velocity $v_{\mathrm{SAW},m}$. In multilayer systems, it is interesting to combine high-velocity, but non-piezoelectric substrates, such as Si, SiC, sapphire and diamond [7–10] with a piezoelectric thin film. Zinc oxide (ZnO) is a very popular piezoelectric thin-film material because of its high electromechanical coupling constant and ease of fabrication. In this work, a ZnO(230 nm)/$SiO_2$(100 nm)/Si multilayer substrate was used. We have deliberately chosen a rather standard (low-resistive) Si substrate to demonstrate that our technology can result

 

in extremely high-frequency SAW devices, which can be monolithically integrated with common electronic circuitry. The $SiO_2$ layer was included, as it was shown that an insulating buffer layer between the piezoelectric film and the substrate also increases the electromechanical coupling [11, 12].

The resolution of standard photolithography (minimum finger width of approximately 0.5 $\mu$m) limits the operation frequency to around a few gigahertz, even for high-velocity substrates [13]. E-beam lithography (EBL) is a good candidate for high-frequency IDTs because of its sub-100 nm resolution. However, the EBL parameters are generally strongly dependent on the substrate properties. This makes it difficult to design a standard lithography procedure for a variety of substrates, apart from reproducibility issues, low throughput and costliness [14, 15].

Nanoimprint lithography is a good candidate for fabricating IDT devices. IDTs on $LiNbO_3$ with center frequencies of 1.488 GHz (170 nm IDT finger width) and 2.38 GHz (130 nm IDT finger width) have been reported with hot embossing NIL and UV–NIL, respectively [16, 17]. A multilayer lift-off process using UV–NIL was also developed to fabricate 140 nm IDT fingers on $LiNbO_3$ [18]. Recently a UV–NIL process with a high-aspect-ratio stamp has been reported to fabricate 100 nm IDT fingers on $LiNbO_3$ with 8.6 GHz center frequency [19]. However, further improvement of the finger resolution of IDTs and reproducibility of the process is limited by the ability to get an appropriate undercut profile, which is essential for metal lift-off.

In this study, an alternative lithography technique, 'step-and-flash nanoimprint lithography' (SFIL), with a novel material system for lift-off, was used to reach very high resolution and higher reproducibility for the fabrication of IDTs. This fabrication method is based on our previous work [20]. While this method has the resolution of EBL, it is basically substrate independent with higher throughput compared to standard EBL.

## 2. Experimental details

Sputtering is the most common deposition method for making polycrystalline ZnO thin films in acoustic applications. In this work, ZnO thin films were deposited on a double side polished (DSP) p-type Si(100) substrate (5–10 Ω cm) with 100 nm thick thermal oxide using an RF magnetron sputtering system with a ZnO target using argon gas (flow 10 sccm) and 50 W RF power at a process pressure of 3 mTorr. During the deposition, the substrate was at room temperature and rotated at 60 rpm to get a uniform film thickness. The ZnO film thickness was measured to be 230 nm by a surface profilometer. An atomic force microscope (AFM) was used to measure the surface roughness. The crystalline structure and grain size of the ZnO film were confirmed by x-ray diffraction (XRD) measurements.

Nanoimprint lithography and a subsequent lift-off process were applied for the high-frequency IDT fabrication. The imprint template used in this work was produced by IMS Chips (Germany), and consisted of IDT devices with finger widths of 125 nm, 100 nm, 80 nm and 65 nm, corresponding to SAW wavelengths of 500 nm, 400 nm, 320 nm and 260 nm, respectively. Figure 1 shows the process steps: first the substrate was spin coated with a ∼80 nm thick PMMA transfer layer (495A 2% from MicroChemicals) at 3000 rpm and baked on a hot plate at 120 °C for 2 min (figure 1(a)). PMMA was used because of its low etching resistance compared to HSQ under oxygen plasma as well as its solubility in standard solvents (e.g. acetone) for easy lift-off. Pattern definition on the $ZnO/SiO_2/Si$ substrate was carried out using SFIL$^{TM}$ on an Imprio$^{TM}$ 55 tool from Molecular Imprints. As imprint material a low-viscosity, organic, and UV-curable resist was used (Monomat$^{TM}$ from Molecular Imprints) by field-to-field dispensing deposition (figure 1(b)). The patterns were replicated by pressing the template into the fluidic resist at room temperature and under low force of 2–3 N (figure 1(c)). After curing the resist through the transparent imprint template using broadband UV light with an exposure dose of 80 mJ $cm^{-2}$ at 230–360 nm wavelength (figure 1(d)), the template was detached leaving its negative replication in the hardened resist (figure 1(e)). For the next step, a planarization layer of ∼160 nm HSQ, XR-1541 6% (from Dow Corning) was deposited by spin coating on top of the imprinted features (figure 1(f)), giving an excellent etch selectivity of more than 1:100 to the imprint and transfer materials. After getting a planarized surface, the etch-back of the overlayer of HSQ (figure 1(g)), and pattern transferring through the residual imprint material and transfer layer that remained after SFIL (figure 1(h)), were performed under $CHF_3$ plasma and $O_2$ plasma, respectively, in a reactive ion etching apparatus (Adixen AMS100DE). For the metallization, ∼25 nm Au with an adhesion layer of Cr (2–3 nm) was grown by using an e-beam evaporation tool (figure 1(i)). Finally lift-off was performed by dipping the sample into acetone followed by ultrasonication (figure 1(j)).

The frequency spectrum characterization of the IDTs was carried out using an Agilent N5244A PNA-X network analyzer. Two-port network analyzer measurements have been performed by using microwave probes (model 40A from GGB Industries) with ground–signal (G–S) and signal–ground (S–G) configuration. The network analyzer was calibrated using a SOLT (short, open, load, through) calibration technique with a calibration substrate (CS-8 from GGB Industries).

## 3. Results and discussion

The thermodynamically stable crystal structure phase of ZnO has wurtzite symmetry with a hexagonal unit cell [21] and shows a preferential growth of *c*-axis (002) perpendicular to the substrate surface, as the ZnO(002) surface has the smallest surface free energy [22]. For SAW applications, highly *c*-axis oriented ZnO films are required because of their higher piezoelectric activity [23]. Figure 2 shows the XRD spectrum of the ZnO film indicating a polycrystalline structure. The (002) peak of ZnO corresponds to the *c*-axis perpendicular to the surface. The additional ZnO(100) peak

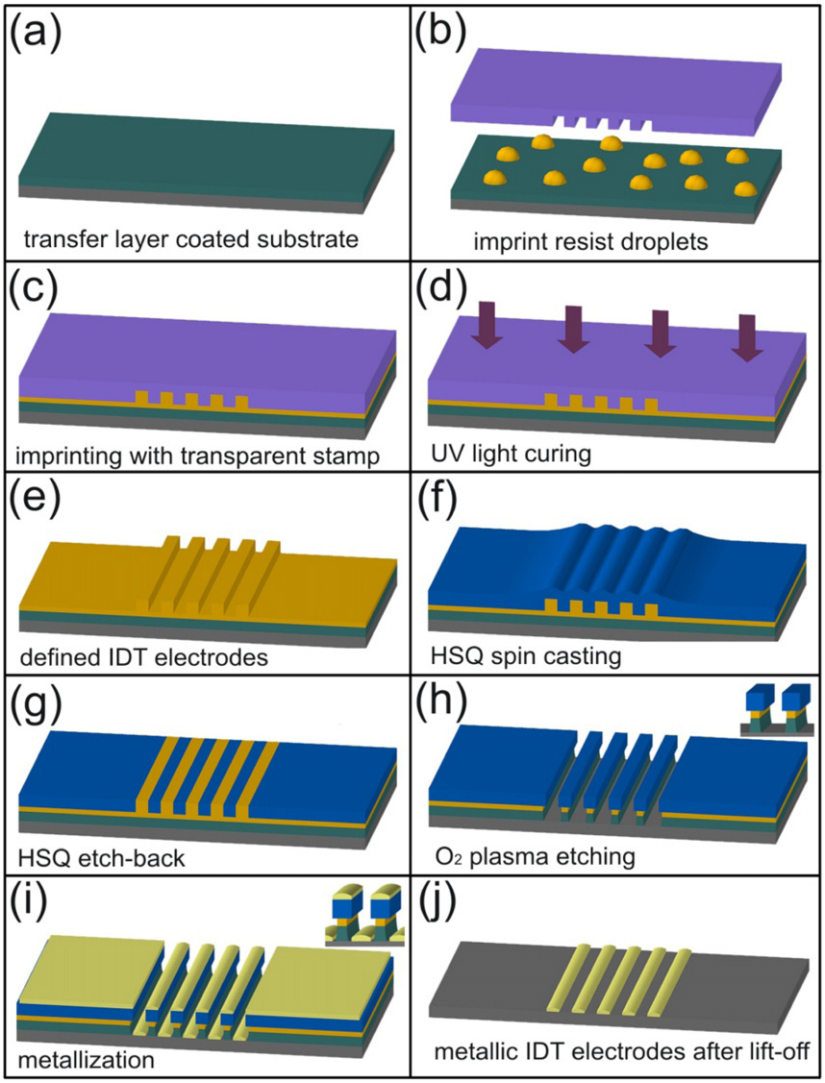


**Figure 1.** Fabrication process flow: (a) coating of the wafer with an organic transfer layer, (b) dispensing of UV-curable, organic imprint material on the surface with local volume adjustment, (c) imprint with a transparent template, (d) UV-light curing of the resist, (e) IDT structures defined in the imprint resist after removal of the template, (f) spin coating of HSQ planarization layer, (g) $CHF_3$ plasma etching of HSQ layer to expose elevated structures in organic layer, (h) $O_2$ plasma etching to transfer pattern down to the substrate, (i) metal deposition by e-beam evaporation, (j) lift-off in acetone.

might be attributed to the granular structure of the film, and it is generally observed at lower growth temperatures and higher Ar:$O_2$ gas mixture ratio [24, 25]. By using the Scherrer formula, we calculated a grain size of around 15 nm. The AFM image shows that the root mean square (rms) roughness of the thin film is 2.5 nm for a 2 $\mu$m $\times$ 2$\mu$m area (inset).

Figure 3 shows SEM images of the IDT device with 65 nm finger width and spacing after nanoimprint lithography. The SFIL process is capable of replicating structures very precisely and reproducibly. From 125 nm down to the 65 nm lines and spaces, the dimensions are successfully transferred into the imprint resist on PMMA.

For further pattern transfer with lift-off, the spin coated HSQ overlayer was etched back under $CHF_3$ plasma. The organic imprint resist layer and transfer layer (PMMA) etching were performed under $O_2$ plasma. As mentioned in the previous section, HSQ plays a very important role for precise pattern transfer through the transfer layer as a planarization and excellent etch mask. It should be noted that uniform HSQ thickness over the sample is required to prevent certain regions on the sample from being exposed by ionic plasma. In other words, HSQ is not only an etch mask for featured areas, but also an etch mask for non-featured areas during $O_2$ plasma etching. In the case of large-scale (a few hundred of microns) continuous shape of the contact pads, the HSQ thickness will be the same on the contact pads and on the non-featured areas (areas away from IDTs) after the spin coating. Such non-uniform thickness of HSQ results in a metallized region around the IDT devices at the end of the fabrication process. Another alternative method, 'HSQ contact planarization' [20], will not be sufficient to remove HSQ over such long distances. In order to have sufficient planarization (uniform HSQ thickness) without additional

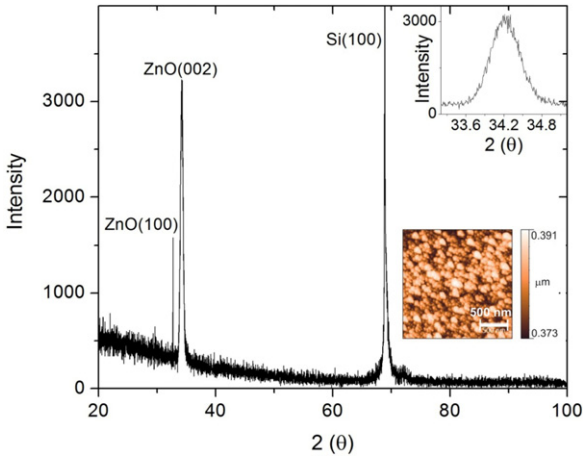


**Figure 2.** XRD pattern and rocking curve of the ZnO(002) peak (upper inset, FWHM 0.54°) showing the accurate *c*-axis orientation of the ZnO layer deposited by rf sputtering on $SiO_2$/Si substrate and AFM image of 2 $\mu$m × 2 $\mu$m ZnO surface indicating an rms surface roughness of approximately 2.5 nm (lower inset).

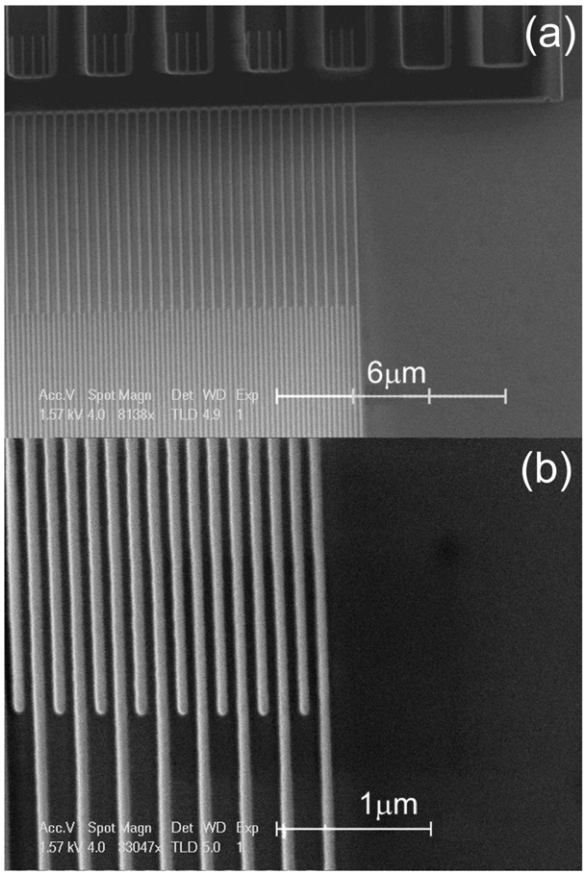


**Figure 3.** (a) SEM image of an imprinted IDT device with line width and spacing of 65 nm, (b) zoom in image of fingers.

**Table 1.** Design parameters of the IDT delay lines.

| | λ (nm) | Number of fingers | Aperture ($\mu$m) | Distance between IDTs ($\mu$m) |
|---|---|---|---|---|
| DL1 | 500 | 1399 | 30 | 405.87 and 1081.87 |
| DL2 | 400 | 1749 | 30 | 405.73 and 1081.87 |
| DL3 | 320 | 2187 | 30 | 405.45 and 1081.87 |
| DL4 | 260 | 2691 | 30 | 405.60 and 1081.87 |

planarization steps to the spin coating, we have used comb shape contact pads for the IDT devices.

Figure 4 shows the optical and SEM images taken after HSQ and transfer layer etching. HSQ provides sufficient planarization for the pattern transfer down to the substrate, preventing non-featured areas (areas away from IDTs) from plasma etching (see figure 1(h)). For successful lift-off, an under-etched side profile is essential. In our previous work, we have already shown that very high etch selectivity between HSQ and underlying organic layers (1:100) provides sufficient under-etched profile for lift-off [20].

In very high-frequency applications, a well defined periodicity and shape of the electrodes have critical importance and determine the device performance. Figure 5 shows SEM images of 125 nm, 100 nm, 80 nm and 65 nm interdigital finger electrodes after metallization and lift-off, demonstrating high regularity and smooth edges of the electrodes, hence very high critical dimension (CD) control of the fabrication process.

In the measured transmission spectrum, the direct electromagnetic coupling (cross-talk) between the generator and receiver IDTs suppresses the acoustoelectric response of the delay line. Moreover, in the case of low-resistivity substrates (<3 kΩ cm), it becomes more difficult to study the transmission spectrum because of the considerable attenuation of the acoustic transmission due to free charges in the silicon substrate [26]. Since the electromagnetic signals travel at the speed of light, i.e. much faster than the SAW velocity, it is possible to separate them from the acoustic ones in a Fourier-transformed spectrum (time domain). A gating technique can be used in the time domain to filter out the crosstalk signal [27]. In this study, the gating technique has been applied for the transmission data presented below.

Figure 6 highlights the capability of our devices to be operated at ultrahigh frequencies. Full design parameters of the IDT delay lines (DLs) are listed in table 1. For each DL, we have observed three resonances in both the reflection and transmission spectrum. Figures 6(a) and (b) show the reflection and transmission spectra of IDTs with 500 nm and 400 nm wavelengths, which hereafter will be referred to as DL1 (delay line 1) and DL2 (delay line 2), respectively. In the frequency spectra, the resonance peak labeled R1 corresponds to the Rayleigh mode with the lowest natural frequency, called the fundamental or first-order Rayleigh mode. Rayleigh surface acoustic modes result from the superposition of a longitudinal and a transverse acoustic mode which is polarized perpendicular to the surface, leading to a displacement field $\mathbf{u} = (u_x, 0, u_z)$ [3]. The modes labeled R2, R3 and R4 are associated with the second-, third- and fourth-order Rayleigh modes, respectively. These higher-order Rayleigh modes normally appear when the acoustic velocity in the overlayers is lower than in the substrate and are determined by the relative thickness of the film ($d_{ZnO}/\lambda_{SAW}$) [7, 11], where the $d_{ZnO}$ is the thickness of the ZnO film. The frequency of these modes depends on

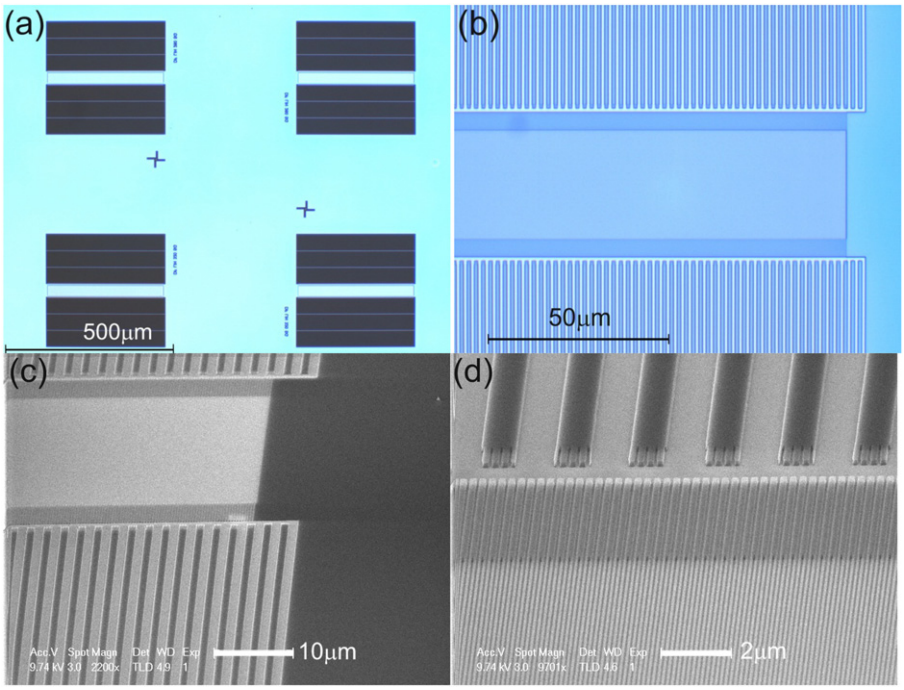


**Figure 4.** Optical ((a), (b)) and SEM ((c), (d)) images of samples after oxygen plasma etching. Light and dark areas in the SEM image correspond to the substrate and the HSQ coated region, respectively.

**Table 2.** Experimental results of resonance frequency, velocity and electromechanical coupling coefficient for different excitation modes of DL1 ($\lambda = 500$ nm), DL2 ($\lambda = 400$ nm), DL3 ($\lambda = 320$ nm) and DL4 ($\lambda = 260$ nm) devices. R1, R2, R3 and R4 are first-order (fundamental), second-order, third-order and fourth-order Rayleigh modes, respectively.

| | R1 | | | R2 | | | R3 | | | R4 | | |
|---|---|---|---|---|---|---|---|---|---|---|---|---|
| DL | $f$ (GHz) | $v$ (m s$^{-1}$) | $k^2$ | $f$ (GHz) | $v$ (m s$^{-1}$) | $k^2$ | $f$ (GHz) | $v$ (m s$^{-1}$) | $k^2$ | $f$ (GHz) | $v$ (m s$^{-1}$) | $k^2$ |
| 1 | 4.697 | 2348 | 0.007 | 8.002 | 4001 | 0.030 | 9.495 | 4747 | 0.010 | — | — | — |
| 2 | 5.737 | 2295 | 0.012 | 9.137 | 3655 | 0.036 | 11.03 | 4412 | 0.014 | — | — | — |
| 3 | — | — | — | 10.54 | 3373 | 0.032 | 12.96 | 4147 | 0.013 | 14.26 | 4563 | 0.025 |
| 4 | — | — | — | 12.17 | 3164 | 0.033 | 15.14 | 3937 | 0.031 | 16.13 | 4194 | 0.028 |

the ratio ($d_{ZnO}/\lambda_{SAW}$) between the overlayer thickness and the acoustic wavelength. The assignment of the observed resonances to Rayleigh modes is substantiated by numerical simulations, discussed below. In our multilayer system, the SAW velocity of the Si substrate is larger than that of both the ZnO and $SiO_2$ layers [28, 29]. Because of the fact that the displacement field of SAWs is confined to a region of around one wavelength from the surface, the layer thicknesses play a crucial role in the response of the IDTs. In the present material system, the ZnO and $SiO_2$ thicknesses are around 230 nm and 100 nm, respectively. One can expect that the reflection of the SAW from the substrate should increase with the further reduction of the acoustic wavelength, which makes excitation of higher Rayleigh modes more likely.

For DL1, the relative thickness ($d_{ZnO}/\lambda_{SAW}$) is 0.46. The first-order Rayleigh mode appears at 4.697 GHz, corresponding to a velocity of 2348 m s$^{-1}$. Higher-order Rayleigh modes have higher velocities and therefore higher resonance frequencies. Second- and third-order modes are observed at 8.002 GHz and 9.495 GHz with corresponding velocities of 4001 m s$^{-1}$ and 4747 m s$^{-1}$, respectively. In the transmission spectrum, the resonance peak of the second-order mode has the highest amplitude, which indicates that the electromechanical coupling constant ($k^2$) of this mode is higher than that of the first and third modes (see table 2). The standard method, described in the IEEE standards, has been used to calculate $k^2$ values from the admittance curves, which were extracted from the reflection data [30].

For DL2, the relative thickness is 0.56 and the first-order Rayleigh mode (R1) appears at 5.737 GHz, corresponding to a velocity of 2295 m s$^{-1}$. The second- (R2) and third-order (R3) modes have resonances at 9.137 GHz and 11.03 GHz, with velocities of 2655 m s$^{-1}$ and 4412 m s$^{-1}$, respectively. The transmission spectrum reveals that the dominant mode is also the second mode for a relative thickness of 0.56.

Figures 6(c) and (d) show both reflection and transmission spectra of the delay lines with 320 nm (DL3) and 260 nm (DL4) wavelength, which is comparable with the distance to the Si substrate from the upper surface of ZnO ($d_{Si} = 330$ nm, $d_{Si}/\lambda_{SAW-DL3} = 1.03$ and $d_{Si}/\lambda_{SAW-DL4} = 1.27$). The resonances observed at 10.541 GHz, 12.959 GHz and 14.260 GHz for DL3 are mediated by the second-order (R2), third-order (R3) and fourth-order (R4) Rayleigh modes, respectively. For DL4, the resonance peaks were observed

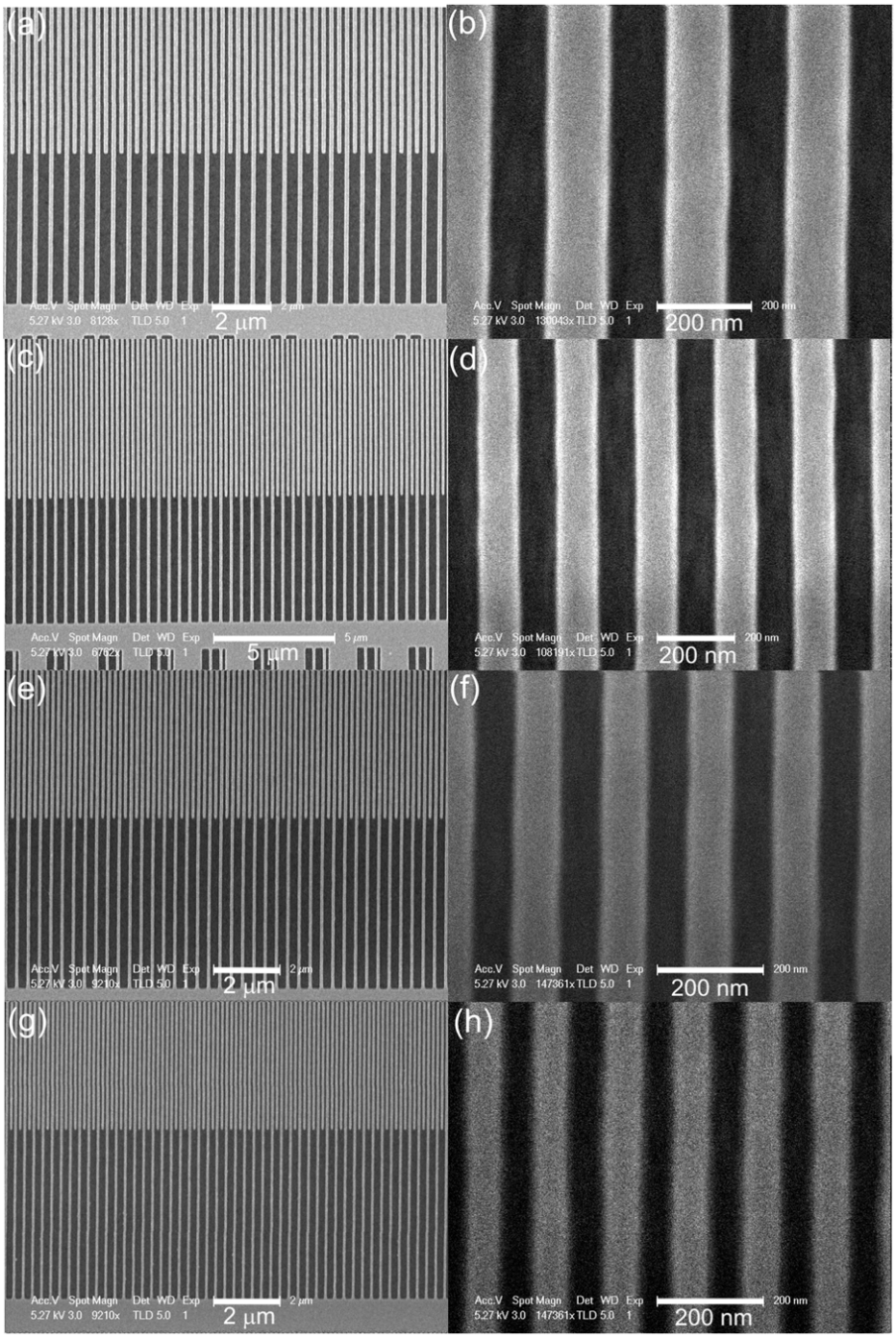


**Figure 5.** SEM images of IDT devices with 25 nm thick Au finger electrodes at the end of the fabrication process: (a) and (b) 125 nm, (c) and (d) 100 nm, (e) and (f) 80 nm, (g) and (h) 65 nm line width and spacing.

at 12.170 GHz (R2), 14.144 GHz (R3) and 16.132 GHz (R4). The absence of the fundamental Rayleigh modes for DL3 and DL4 might be explained by the low value of the electromechanical coupling coefficient of the fundamental Rayleigh modes for these wavelengths.

For the device operation, especially at very high frequencies, not only the velocity and electromechanical coupling coefficient, but also the acoustic propagation loss, is important. SAW scattering at the grain boundaries of the ZnO film is one of the main reasons for propagation loss. Propagation loss depends on the ratio of the wavelength to the grain size, and decreases with decreasing grain size [31]. At very high frequencies, propagation loss is expected to be high due to the exponential dependence on frequency. To study propagation loss of the SAW modes in our devices, we have used delay lines with different separations between input and output IDTs. Insertion losses (transmission spectra) were measured for each device with two different separations (see figure 6). By using the dB difference between resonance peak values ($|\alpha_2| - |\alpha_1|$) and propagation distances (405.87 and 1081.87 $\mu$m), we calculated propagation losses for different acoustic wavelengths and modes. Figure 7 shows the

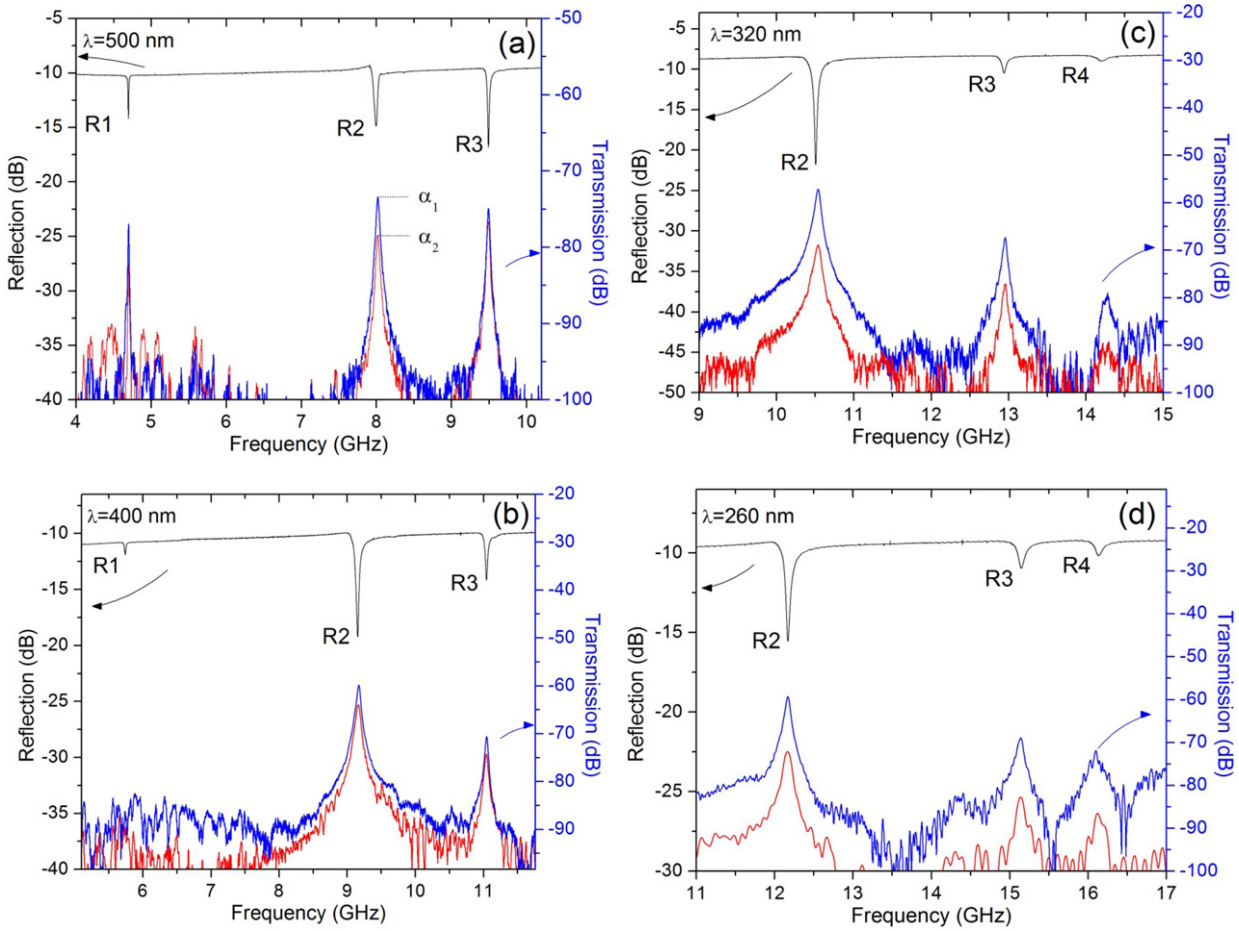


**Figure 6.** IDT reflection and transmission spectra for (a) DL1 ($\lambda = 500$ nm), (b) DL2 ($\lambda = 400$ nm), (c) DL3 ($\lambda = 320$ nm) and (d) DL4 ($\lambda = 260$ nm). The peaks labeled R1, R2, R3 and R4 correspond to the fundamental Rayleigh mode, second-order Rayleigh mode, third-order Rayleigh mode and fourth-order Rayleigh mode, respectively. Two different transmission curves were measured from IDTs with different separations. Blue (upper) curves, measured from ∼405 $\mu$m separated IDTs; red (lower) curves, measured from ∼1081 $\mu$m separated IDTs.

propagation losses in units dB mm$^{-1}$. For the first mode (R1) of DL2, we are not able to measure a clear difference between the resonance peaks because of the residual cross-talk signal at this frequency. Figure 7 reveals that the R3 mode of DL1 has a minimum loss of ∼2.6 dB mm$^{-1}$ ($13 \times 10^{-4}$ dB/λ). Maximum propagation loss was calculated for the R4 mode of DL4, which is ∼22 dB mm$^{-1}$ ($58 \times 10^{-4}$ dB/λ). As illustrated in figure 7, the propagation losses for the same type of mode in different delay lines tend to increase with frequency. It is found that for R2 and R3 the propagation losses are weakly frequency dependent until around 9 GHz and 11 GHz, respectively.

The assignment of the SAW modes was confirmed by finite element method (FEM) calculations, using COMSOL®Multiphysics software. Eigenfrequency analysis was used to determine the resonance frequencies and the modes of deformation in the multilayer system. The material parameters used in the calculations are given in table 3. As the IDTs have a large number of fingers, and the length of these fingers is a few hundred times longer than their width, edge effects can be neglected. Therefore, the finger pairs can be regarded as an infinitely extended periodic structure and

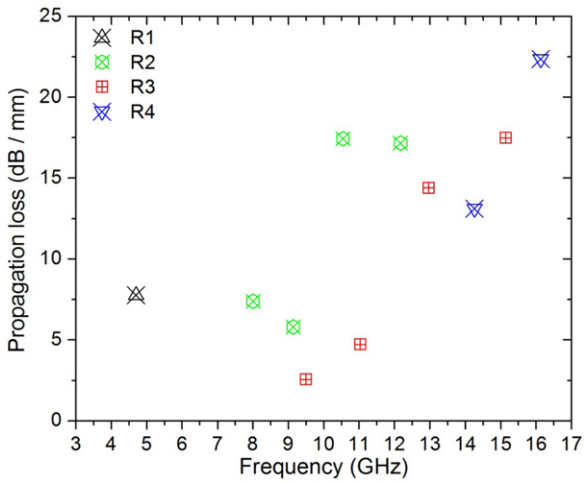


**Figure 7.** Propagation losses for Rayleigh wave modes in delay line devices as a function of frequency.

the model geometry can be reduced to one wavelength [32]. The geometries used in the model are given in figures 8 and 9 with the results. The SAW propagation direction was

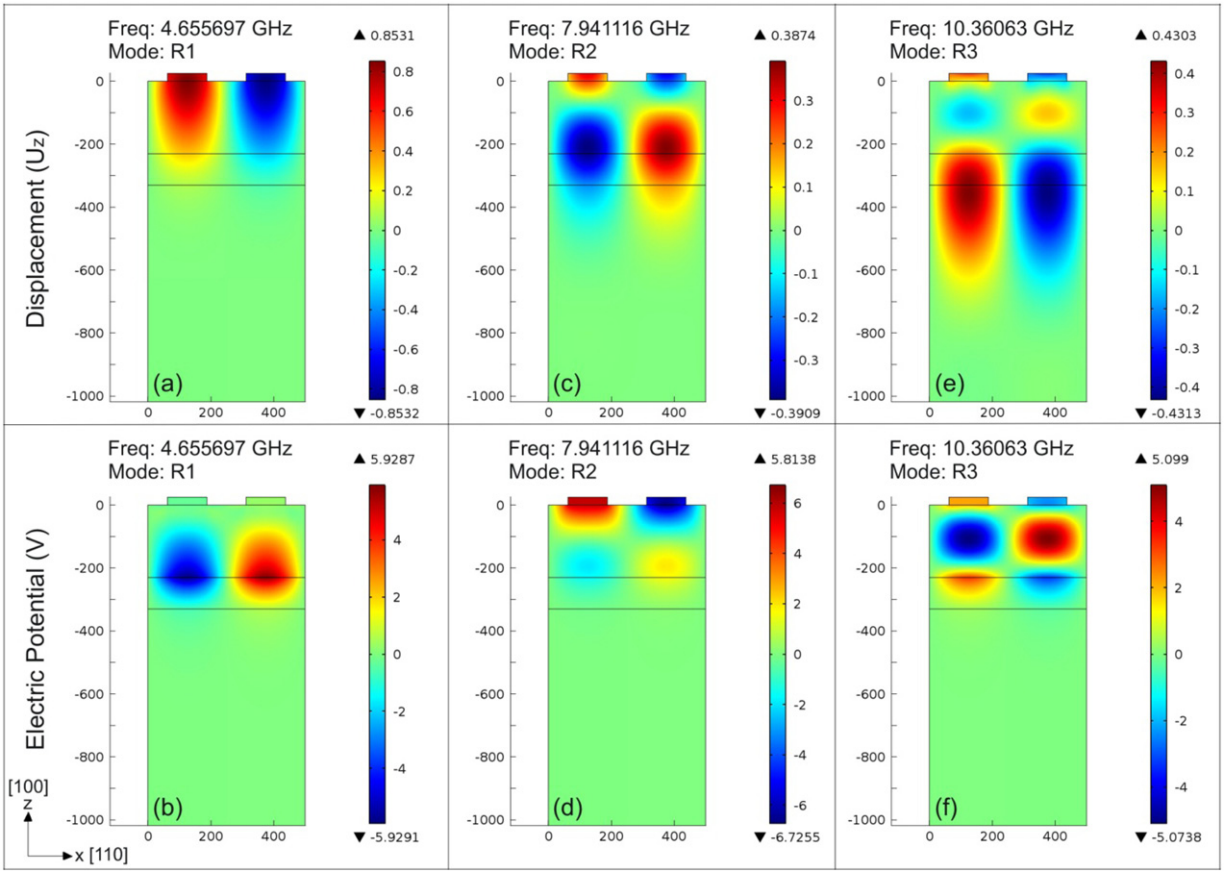


**Figure 8.** FEM calculation results for DL1 ($\lambda = 500$ nm). The upper row shows the vertical component of the displacement field for R1, R2 and R3 modes (left to right). The lower row shows the electric potential distribution in the ZnO(230 nm)/$SiO_2$(100 nm)/Si multilayer for R1, R2 and R3 modes (left to right). The numbers on the colored legend have arbitrary units.

chosen along the $x$-axis corresponding to the [110] crystal direction of the silicon substrate. The vertical component of the displacement field and the corresponding electric potential distribution were used to define the piezoelectrically active surface acoustic modes. Certain calculated modes, which yield a symmetric displacement ($u_z$) along the $x$-axis and a reversely polarized electric potential on the fingers, were assigned as piezoelectrically active. This confirms that these modes can be excited by using reversely polarized finger pairs (as in an IDT) via the inverse piezoelectric effect.

In figure 8, simulation results for an IDT with 500 nm wavelength (DL1) are presented. R1, R2 and R3 modes appear at 4.656 GHz, 7.941 GHz and 10.361 GHz, respectively. The displacement field of the fundamental Rayleigh mode (R1) is mostly concentrated in the 230 nm thick ZnO layer, and it completely vanishes in a distance of one wavelength (figure 8(a)). The electric potential profile for the same mode exhibits a symmetric distribution along the $x$-axis (figure 8(b)). The potential around the ZnO/$SiO_2$ interface is higher than on the electrodes, which implies that the induced potential in this region will be higher than the applied potential on the finger electrodes during IDT operation. Higher-order Rayleigh modes are characterized by the number of displacement nodes (minimal amplitude points) in the $z$-component of the displacement field along the vertical direction ($z$-axis). The displacement field of the second mode (R2) penetrates more into the substrate than the first mode (figure 8(c)). The node along the $z$-axis which appears in the ZnO layer denotes the second-order Rayleigh mode (R2). The symmetric potential distribution of the R2 mode also has a node in the ZnO layer and has its maximum value on the finger electrodes (figure 8(d)). The penetration depth of the

**Table 3.** Material constants used for FEM analysis.

| Material | | Au | ZnO | $SiO_2$ | Si |
|---|---|---|---|---|---|
| Density (kg $m^{-3}$) | $\rho$ | 19 300 | 5665 | 2350 | 2330 |
| Elastic constants (Pa $\times 10^{11}$) | $C_{11}$ | 2.202 | 2.0900 | 0.785 | 1.944 |
| | $C_{12}$ | 1.604 | 1.2035 | 0.161 | 0.352 |
| | $C_{13}$ | 1.604 | 1.0460 | 0.161 | 0.639 |
| | $C_{33}$ | 2.202 | 1.6570 | 0.785 | 1.657 |
| | $C_{44}$ | 0.299 | 0.4230 | 0.312 | 0.796 |
| | $C_{66}$ | 0.299 | 0.4440 | 0.312 | 0.509 |
| Piezoelectric constants (C $m^{-2}$) | $e_{15}$ | — | −0.480 | — | — |
| | $e_{31}$ | — | −0.573 | — | — |
| | $e_{33}$ | — | 1.321 | — | — |
| Relative permittivity | $\epsilon_{11}$ | — | 7.38 | 2.37 | 11.68 |
| | $\epsilon_{33}$ | — | 7.38 | 2.37 | 11.68 |

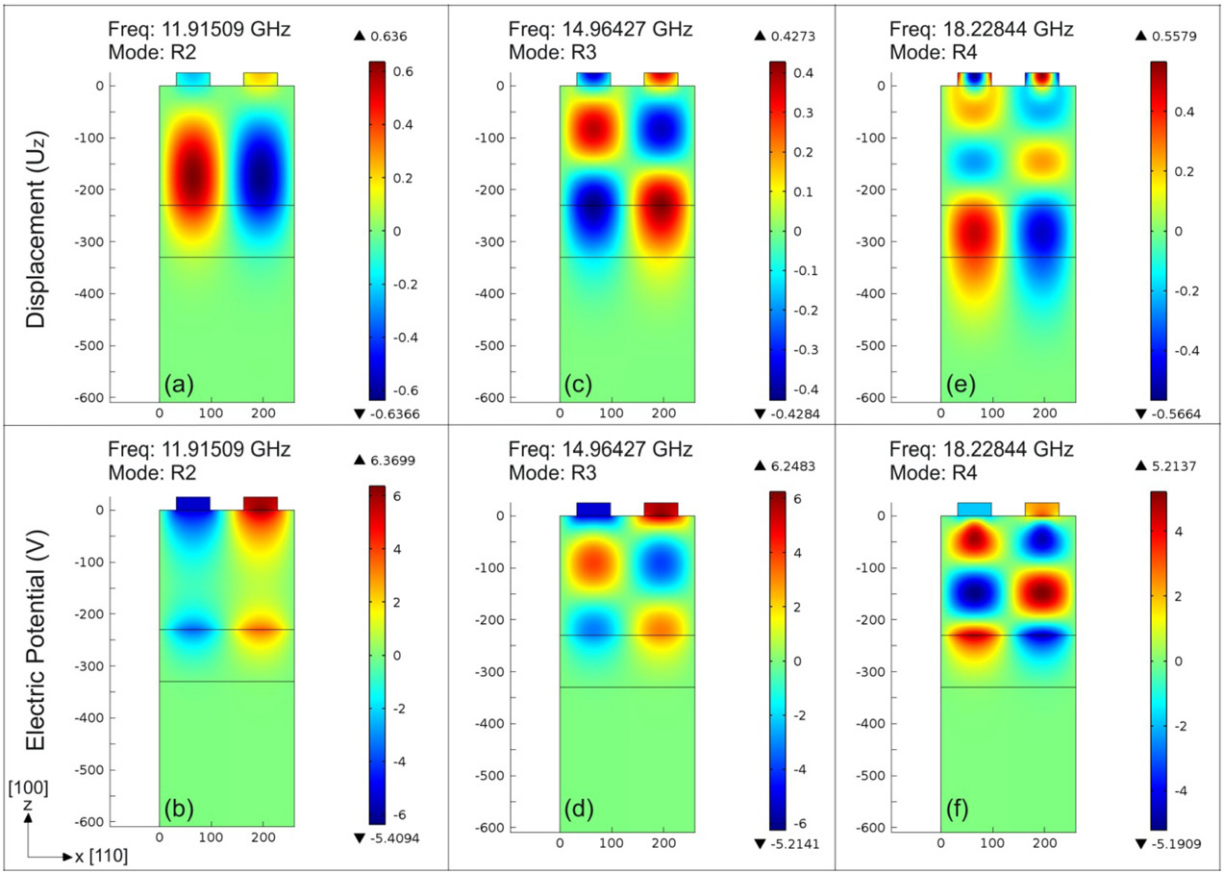


**Figure 9.** FEM calculation results for DL4 ($\lambda = 260$ nm). The upper row shows the vertical component of the displacement field for R2, R3 and R4 modes (left to right). The lower row shows the electric potential distribution in the ZnO(230 nm)/$SiO_2$(100 nm)/Si multilayer for R2, R3 and R4 modes (left to right). The numbers on the colored legend have arbitrary units.

displacement field reaches a maximum for the third mode (R3), exhibiting two nodes in the ZnO layer (figure 8(e)) and the maximum value of the electric potential appears in the ZnO layer (figure 8(f)).

The simulation results for an IDT with 260 nm wavelength (DL4) can be seen in figure 9. One can derive that, in contrast to DL1, the lowest excited resonance frequency for DL4 corresponds to the second-order Rayleigh mode (R2), and it appears at 11.915 GHz (figures 9(a) and (b)). The other calculated resonances, at 14.964 GHz and 18.228 GHz, correspond to the R3 mode (figures 9(c) and (d)) and R4 mode (figures 9(e) and (f)), respectively. The calculated displacement field and electric potential profiles for all devices confirm that the modes are all piezoelectrically active. In other words, the corresponding type of deformation can be excited by IDTs.

A comparison of the measured and calculated modes for all IDT devices is given in figure 10 with the relative difference between them as a percentage. The calculated frequencies are in very good agreement with the measured values, especially for the fundamental (R1) and second-order (R2) modes. The deviation between experiment and simulation for the R3 and R4 modes can possibly be attributed to the uncertainties in the ZnO properties.

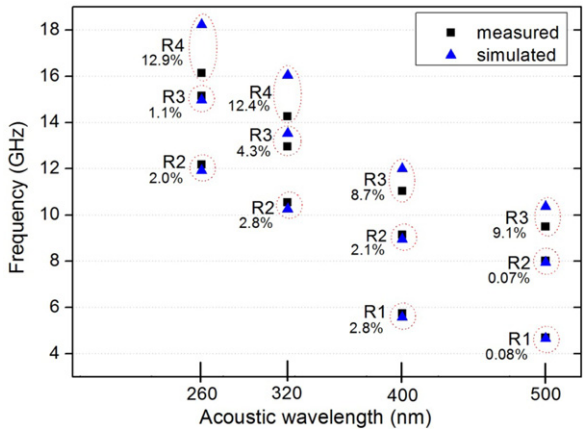


**Figure 10.** Comparison of the frequencies obtained experimentally and numerically for all IDT devices with their difference as a percentage. R1, R2, R3 and R4 labels represent the fundamental (first-order), second-order, third-order and fourth-order Rayleigh modes, respectively.

## 4. Conclusion

In conclusion, we have fabricated ultrahigh-frequency IDTs on a ZnO/$SiO_2$/Si multilayer system, using nanoimprint lithography, and performed electrical characterization. Crucial

to our novel approach is the application of a hydrogen silsesquioxane (HSQ) layer that provides excellent planarization combined with very high etching selectivity, critical dimension control and easy lift-off. The highest resonance frequency reported so far for ZnO-based transducers on silicon (16.1 GHz) was measured on an IDT with 65 nm finger width. Our experimental results are in very good agreement with numerical simulations of the specific multilayer system. The IDT performance is expected to improve after optimizing the ZnO growth parameters and lowering the Si substrate conductivity. Our technology has great potential to reach even higher frequencies in the case of higher velocity substrates, such as SiC, sapphire or diamond.

## Acknowledgments

The authors would like to thank Assistant Professor Dr Yusuf Selamet for access to the RF sputtering system at the Physics Department of the İzmir Institute of Technology, Turkey; Professor Dr Bram Nauta for access to his laboratory, Henk de Vries for helping with the RF measurements, and Hadi Yagubizade for discussions on modeling. This research was performed within the NanoArrays project financed by The Netherlands Technology Foundation STW.

## References

[1] Michael J V 1998 *Ultrasonics* **36** 7
[2] Rocke C, Zimmermann S, Wixforth A and Kotthaus J P 1997 *Phys. Rev. Lett.* **78** 4099
[3] Lima M M D Jr and Santos V P 2005 *Rep. Prog. Phys.* **68** 1639
[4] Talyanskii V I, Shilton J M, Cunningham J, Pepper M, Ford C J B, Smith C G, Linfield E H, Ritchie D A and Jones G A C 1998 *Physica* B **249–251** 140
[5] Sogawa T, Santos P V, Zhang S K, Eshlaghi S, Wieck A D and Ploog K H 2001 *Phys. Rev. Lett.* **87** 276601
[6] Campbell C K 1989 *Proc. IEEE* **77** 1453
[7] Takagaki Y, Santos P V, Wiebicke E, Brandt O, Schönherr H-P and Ploog K H 2002 *Phys. Rev.* B **66** 155439
[8] Takagaki Y, Santos P V, Wiebicke E, Brandt O, Schönherr H-P and Ploog K H 2002 *Appl. Phys. Lett.* **81** 2538
[9] Wu T-T and Wang W-S 2004 *J. Appl. Phys.* **96** 5249
[10] Nakahata H, Higaki K, Hachigo A, Shikata S, Fujimori N, Takahashi Y, Kajihara T and Yamamoto Y 1994 *Japan. J. Appl. Phys.* **33** 324
[11] Srivastava R and Mansingh A 1988 *J. Phys. D: Appl. Phys.* **21** 1535
[12] Shih W-C, Wu M-S, Shimizu M and Shiosaki T 1993 *IEEE Trans. Ultrason., Ferroelectr. Freq. Control.* **40** 642
[13] Nakahata H, Fujii S, Higaki K, Hachigo A, Kitabayashi H, Shikata S and Fujimori N 2003 *Semicond. Sci. Technol.* **18** 96
[14] Muller A, Neculoiu D, Konstantinidis G, Deligeorgis G, Dinescu A, Stavrinidis A, Cismaru A, Dragoman M and Stefanescu A 2010 *IEEE Electron. Device Lett.* **31** 1398
[15] Iriarte G F, Rodriguez-Madrid J G and Calle F 2012 *J. Mater. Process. Technol.* **212** 707
[16] Takagaki Y, Wiebicke E, Kostial H and Ploog K H 2002 *Nanotechnology* **13** 15
[17] Cardinale G F, Skinner J L, Talin A A, Brocato R W, Palmer D W, Mancini D P, Dauksher W J, Gehoski K, Le N, Nordquist K J and Resnick D J 2004 *J. Vac. Sci. Technol.* B **22** 3265
[18] Le N V, Gehoski K A, Dauksher W J, Baker J H, Resnick D J and Dues L 2005 *Proc. SPIE* **5751** 219
[19] Chen N H, Huang J C, Wang C Y and Huang F S 2011 *J. Micromech. Microeng.* **21** 45021
[20] Büyükköse S, Vratzov B and van der Wiel W G 2011 *J. Vac. Sci. Technol.* B **29** 021602
[21] Özgür Ü, Alivov Ya I, Liu C, Teke A, Reshchikov M A, Doğan S, Avrutin V, Cho S-J and Morkoç H 2005 *J. Appl. Phys.* **98** 41301
[22] Fujimura N, Nishihara T, Goto S, Xu J and Ito T 1992 *J. Cryst. Growth* **130** 269
[23] Hickernell F S 1985 *IEEE Trans. Sonics Ultrason.* **32** 621
[24] Kim K S, Kim H W and Lee C M 2003 *Mater. Sci. Eng.* B **98** 135
[25] Singh R, Kumar M and Chandra S 2007 *J. Mater. Sci.* **42** 4675
[26] Heinrich W, Gerdes J, Schmuckle F J, Rheinfelder C and Strohm K 1998 *IEEE Trans. Microw. Theory Technol.* **46** 709
[27] Clement M, Vergara L, Sangrador J, Iborra E and Sanz-Hervas A 2004 *Ultrasonics* **42** 403
[28] Slobodnik A J, Conway E D and Delmonico R T 1973 *Microwave Acoustics Handbook* (*Bulk Wave Velocities*) vol 3 (Spring field, VA: National Technical Information Service, US Department of Commerce)
[29] Hadjoub Z, Beldi I and Doghmane A 2007 *C. R. Physique* **8** 948
[30] *IEEE Standard on Piezoelectricity-Std* 1988 (New York: The Institute of Electrical and Electronics Engineers, Inc) 176–1987
[31] Papadakis E P 1965 *J. Acoust. Soc. Am.* **37** 703
[32] Zhao Y G, Liu M, Li D M, Li J J and Niu J B 2009 *Sensors Actuators* A **154** 30